ELSEVIER

Aerosol Remote Sensing Using Ground-Based Measurements and POLDER Airborne Sensor above Coastal Waters

M. Chami and R. Santer**

We conducted in 1994 and 1995 several airborne campaigns with an aircraft version of the POLDER (POLarization and Directionality of Earth Reflectance) instrument. We flew over the Straits of Dover. The main goal of this activity was to see how well we can characterize the atmospheric aerosols using POLDER data in order to achieve atmospheric corrections for ocean color purposes. We also set up atmospheric measurements (solar extinction, sky radiance, and degree of polarization) on which we tested classical aerosol models (Junge size distribution; Shettle and Fenn, 1979) for retrieval. For standard meteorological visibilities, such models allow correct matching of the measurements. For most turbid days, it is shown that a submicron particles haze can be superposed to the continental aerosol background. But we indicated that the SF models enable a good retrieval of the measurements. They thus appear relevant to describe more complex situations. Classically, we first used POLDER images to select an aerosol model based on the spectral dependence of the aerosol reflectance between the red and the infrared for which the water is dark offshore of the Straits. Compared again to the SF models, the spectral dependence observed differ substantially by large angular variations. A detailed analysis showed that these large dispersions are not related to instrumental noise but to natural variation of the aerosols and to residual errors in the Fresnel reflection correction. By averaging, we can also propose SF models. Both ground-based and POLDER-derived aerosol models are consistent in terms of retrieval of the atmospheric functions required for atmospheric corrections. We also tried less successfully a selection based on the polarized reflectance which is a POLDER capability. ©*Elsevier Science Inc., 1998*

INTRODUCTION

In the framework of ocean color observations, the upward signal coming from the surface reached by a satellite is very low. Sturm (1981) provides a typical example (Table 1) of the contribution of each component in the total signal received by a sensor. It clearly appears that the atmospheric radiance is the bulk of the upward signal especially in the red end of the visible spectrum. In these conditions, the atmospheric correction over such target is a critical problem.

In the open ocean, the atmospheric correction scheme applied is based on the darkness of the water in the red and near-infrared part of the visible spectrum. For the CZCS (Coastal Zone Color Scanner) experiment (1978) (Hovis et al., 1980), there is no band in the near-infrared and only the red band was primary used to get information on the aerosols (Bricaud and Morel, 1987). Because of this limitation, the information was very crude: To extrapolate the aerosol reflectance in the blue, we then needed to assume an aerosol model mainly to get a spectral dependence.

For the recent and future ocean color missions, the red and infrared bands are available. The spectral variation of the aerosol reflectance, so-called Gordon coefficient ε (the ratio of the aerosol reflectance between 670 nm and 875 nm), measured by the sensor is compared for the direction of observation to ε coefficients computed for different standard models (Shettle and Fenn, 1979; WMO, 1986). The aerosol model is then selected and applied to the satellite data to correct for atmospheric effects. Gordon and Wang (1994) proposed an

* Laboratoire d'Optique Atmosphérique, Université du Littoral Côte d'Opale, Station Marine de Wimereux, Wimereux, France

Address correspondence to M. Chami, Lab. d'Optique Atmosphérique, Univ. du Littoral Côte d'Opale, L.I.S.E., BP 59, 62930 Wimereux, France. E-mail: chami@loalit.univ-littoral.fr

Received 22 May 1997; revised 27 April 1998.

REMOTE SENS. ENVIRON. 66:203–221 (1998)

655 Avenue of the Americas, New York, NY 10010

0034-4257/98/$–see front matter
PII S0034-4257(98)00047-9

Table 1. Typical Contribution of the Water Leaving Radiance (L_w), Atmospheric Radiance (L_{atm}) and Sunglint Radiance (L_g) to the Signal Reached by a Satellite Sensor (Sturm, (1981)

	Contribution to the Total Signal (%)					
	Clear Water			*Turbid Water*		
nm	L_w	L_{atm}	L_g	L_w	L_{atm}	L_g
440	14.4	84.4	1.2	18.1	80.8	1.1
520	17.5	81.2	1.3	32.3	66.6	1.1
550	14.5	84.2	1.3	34.9	64.1	1.0
670	2.2	96.3	1.5	16.4	82.4	1.2
750	1.1	97.0	1.9	1.1	97.4	1.5

algorithm based on this characterization of the aerosols for SeaWiFS (Sea Wide Field of view Sensor). Improvements of the previous algorithm were proposed by taking into account the multiple scattering process and coastal waters case by adding specific coastal aerosol models. This scheme is suggested for OCTS (Ocean Color Temperature Scanner), MERIS (MEdium Resolution Imaging Spectrometer), and POLDER experiments. In the case of the POLDER algorithm, the directionality is simply used to average the Gordon coefficient.

Coastal waters highly differ from global ocean. The medium is much more complex in the water column as well as in the atmosphere. The water content in dissolved and suspended material is higher due to the pouring of the flows in the sea. Likewise, the sea–land interface may play a role in the local climatology of the aerosols. The mixing of continental and maritime particles may disturb the behavior of the aerosols commonly observed in the global ocean. Nevertheless, Schwindling (1996) reported that the aerosols observed in Southern California can be easily identified by reference to standard aerosol models with a direct relationship between the Angström exponent α and ε.

Several field experiments occurred in the Straits of Dover (France) in 1994 and 1995 and each time, an airborne version of the POLDER sensor was used. In this article, we lead an analysis of aerosol properties with the help of optical measurements in a coastal environment highly influenced by hazes. Another goal is to study how efficient the standard atmospheric correction algorithms are in coastal zones and to assess POLDER contributions face to such medium. A possible improvement of these schemes is discussed considering the directionality and polarization properties of POLDER.

FIELD MEASUREMENTS

Materials

The methodology consists of using POLDER aircraft data over the sea surface and ground measurements. The optical thickness data are given by a radiometer developed by the Cimel Electronic company working at 440 nm, 670 nm, 870 nm, and 1020 nm.

An instrument designed at the Laboratoire d'Optique Atmosphérique of Lille (LOA) (France), REFPOL (REFlectancemètre POLarisé), was used to measure sky and water leaving radiances. This radiometer works at four wavelengths centered at 450 nm, 650 nm, 850 nm, and 1650 nm. The bandwidths are 40 nm in the visible spectrum and 100 nm at 1650 nm. Polarizers located every 45° enable us to get polarized and total radiance measurements. REFPOL usually operates in the principal plane where it scans from the ground to the sky and vice-versa when it comes back in its initial position (Fig. 1). A quite substantial amount of work was devoted on the use of the polarization to characterize the aerosols. The starting point was to use optical thickness measurements as well as almucantar measurements (Deuzé et al., 1988) to describe the size distribution regardless of the particle refractive index and then to determine this parameter based on the large sensitivity of the polarization to it.

As often as possible, POLDER measurements over the sea were coupled to ground measurements. The POLDER concept is detailed in Deschamps et al. (1994). It is a CCD matrix with a wide field of view ranging from 42° in the across track direction to 51° in the along track direction. In this case, its filter wheel acquires measurements at 443 nm, 500 nm, 570 nm, 670 nm, and 870 nm in radiance. The blue and near-IR spectral bands (443 nm and 870 nm) are supplied with polarizers. POLDER was used for the first time over the study area in an airborne version developed at the LOA (Deuzé et al., 1993). The principle view of this sensor enables us to get a sampling of the bidirectional reflectance distribution function (BRDF) of pixels as the plane moves. One ground pixel is typically viewed under nine different angles. Several scenes were taken in 1994 and 1995 and the plane followed the ship along an inshore–offshore transect. The flight altitude was about 2000 m and the sensor acquired a set of data every 7 s. The rotation period of the filter wheel is about 4 s and the speed was typically 70 m s^{-1}. The footprint is about 15 m×20 m

Figure 1. Operating mode of the REFPOL instrument for sky measurements.

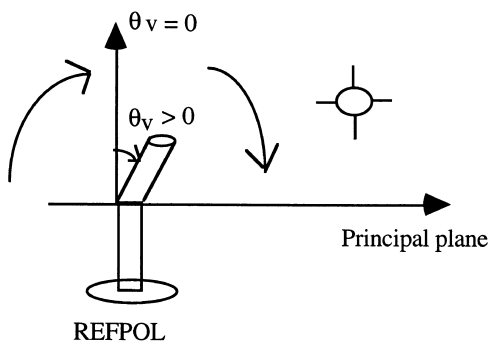

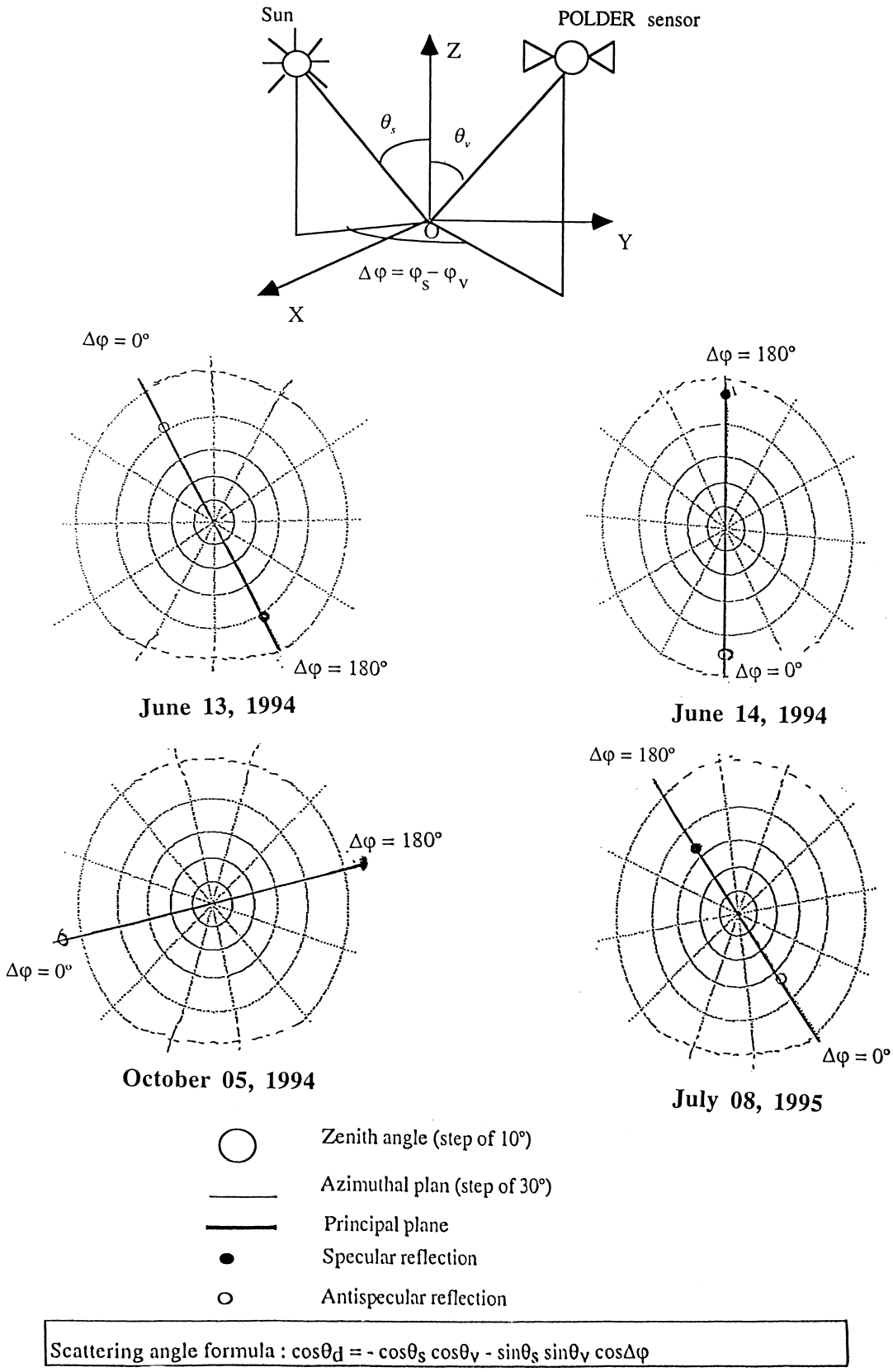

Figure 2. Observation geometrical conditions of POLDER scenes for the day of measurements. The representation is given in azimuthal and zenith angles. We indicated the formula to obtain the correspondence in scattering angle.

and the final images are partitioned in 242×288 ground pixels. The plane moves of about 30 m from one spectral band to another when there are no polarizers and about 120 m with polarizers. The registration of POLDER images does not appear critical since the atmosphere could be considered as spatially homogenous for such distance. Moreover, as will be seen later, the images are smoothed so that it reduces considerably possible errors related to the registration particularly if we use a combination of the spectral bands 670 nm and 870 nm. Figure 2 reports the geometrical conditions of POLDER acquisitions (offshore scenes) for all the days of measurements. The specular reflection generally occurs for a scattering angle ranging from 90° to 110°.

REFPOL and POLDER were calibrated before and after the field experiment at the LOA with an integrating sphere. The calibration accuracy of POLDER is 5%. The given values are normalized to an extraterrestrial irradiance E_s equal to PI that means that the radiance is calculated according to the formula: $L_{\text{norm}}=L_{\text{real}}*(\text{PI}/E_s)$. A comparison between laboratory calibration and sun calibration of REFPOL is given by Cosnefroy et al. (1997) which leads to believe that the calibration is within the 5% range accuracy.

MEASUREMENTS

Site of Measurements

Three field experiments occurred from June 1994 to July 1995 at Wimereux (France) in the Straits of Dover (Fig. 3). Two summer experiments (June 1994 and July 1995) had the objectives to remotely sense chlorophyll pigment; a third one, in autumn (October 1994), had the goal to study suspended sediments, the main source of particles during equinox tides.

This coastal area is the work zone of the biologist group of the Station Marine de Wimereux. It has important hydrologic features and the water can be considered as a Case II classification type. Case II waters are seas whose optical properties are dominated by non-chlorophyll-related sediments or yellow substance instead of, or in addition to, phytoplankton. The water bodies are well distinguished from each other, and their signature is highly correlated with continental effects. Previous studies (Dupont et al., 1981; Bentley, 1985) showed that the coastal waters are clearly dissociated from open ocean through their salinity, turbidity, and their abundance in phytoplancton. The chlorophyll pigment concentration often exceeds 10 μg/L inshore. A frontal zone separates these two water types, and convergence motions are observed. This front acts as an obstacle for the migration of the particles to the offshore waters and prevents them from leaving the coastal area.

The medium is not very deep, with a maximum of 50 m in the middle of the Straits.

Weather Conditions

Temperature

This is a key parameter that may help to understand the various mechanisms responsible for the circulation of the air masses. For instance, the "sea breeze" during the day and the "land breeze" during the night are strictly related to thermal effects between the continent and the ocean. In the same way, an air mass that cools at the same pressure (at sea level, for example) is going to give rise to a local haze above the sea which strongly increases the turbidity of the medium. In Wimereux, numerous hazes are observed especially in summer. The process described as follows could be one possible explanation: The temperature decreases at sea level when the sun sets so that the dew point is reached at night. Then condensation occurs and droplets grow up. A haze appears and persists at night above the sea. The day after, the sun warms up the continent faster than the ocean, and convective motions develop so that the atmosphere warms up too. The temperature of the ocean is too low to generate these motions above it, and the haze still goes on during the day until the temperature is high enough to warm up the atmosphere. Another explanation would consist in considering the horizontal displacement of an air mass from the continent. The condensation would appear as soon as this air mass passes over the ocean with a lesser temperature and would lead to a haze. The temperatures of the different days of measurements are listed in Table 2. The noticeable sea–land gradient behaves with a continent warmer than the ocean in summer. The contrary is observed in October and may validate the processes mentioned above.

Horizontal Visibility—Wind—Relative Humidity

A clear sky is necessary to describe the atmosphere in term of aerosols and to quantify their abundance. The horizontal visibility is also a first flag to assess the turbidity of the medium. On 13 June 1994, there were few cirrus clouds over the site where POLDER flew. It was coupled to optical depth acquisitions carried out on the roof of the Station Marine de Wimereux. Unfortunately, the sea was too rough to get REFPOL scannings on the boat SEPIA II, a CNRS (Centre National de la Recherche Scientifique) research vessel. Sky radiance was only measured once REFPOL came back to the Station Marine. The day after was clearer, and all kinds of measurements were collected (water leaving radiance, sky radiance, and degree of polarization from REFPOL, optical depth data, and POLDER overpass). On 5 October 1994, the day of the POLDER flight, turbidity increased during the day but was still low enough to get data. The rough-

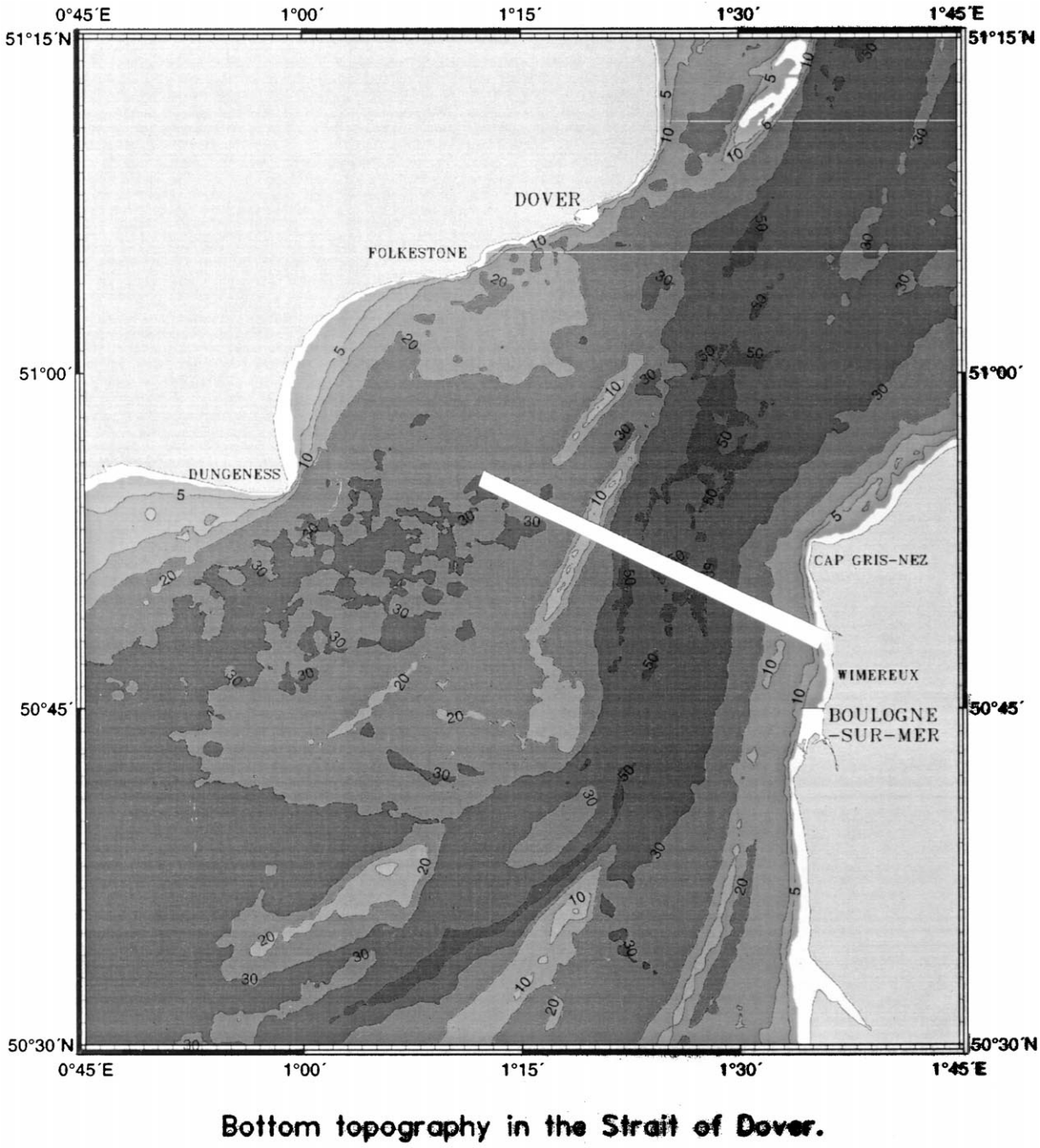

Figure 3. Location of the experiment. The transect offshore of Wimereux corresponds to boat samples. An aircraft leg follows this transect E–W. Two other legs parallel to the coastline were flown by aircraft.

ness of the sea did not enable the boat to leave the port. This was done the day after. The last day of POLDER acquisition was on 8 July 1995. A very clear sky started the day, and a haze grew up so that the experiment ended at 15 h 30 min UTC, the horizontal visibility being less than 8 km. Table 3 reports these visibilities.

Since the wind is responsible for sea roughness, the magnitude of the direct reflected solar beam is a function of wind speed (direct sunglint). Moreover, this factor could provide clues regarding the evolution of hazes during the day. Table 3 gives the various wind speeds and wind directions. A north component is often observed in the site.

The variation of the relative humidity with respect to the time supplies pieces of information about the density of the hazes. The values reported in Table 3 were measured in Boulogne sur Mer (France). If the relative humidity decreased on 13 June 1994 during the day, a

Table 2. Temperature along the Cruise Transect from the Continent to the Ocean

	Continent Temperature (°C)	*Sea Temperature (Inshore) (°C)*	*Sea Temperature (Offshore) (°C)*
13 June 1994	14.0	13.0	12.4
14 June 1994	14.9	13.4	12.8
5 October 1994[a]	9.9	15.4	15.8
8 July 1995	18.2	16.7	15.2

[a] The sea temperature are those of 6 October, which is the date of the cruise measurements.

noticeable increase (from 60% to 78%) occurred on 14 June confirming the apparition of hazes. In July 1995, a strong value (around 70%) persisted all day, and the coupling with a low sea temperature may have generated the growth of hazes above the sea surface.

Atmospheric Measurements

Optical Thickness

The atmosphere was generally too unstable during the different campaigns, and the Langley method could not be applied to get the mean optical depth. So we retrieved the instantaneous optical thicknesses from the calibration coefficients derived routinely with the Langley plot for more stable days. We plotted Figure 4 aerosol optical depth τ_a at 550 nm corrected for Rayleigh and ozone absorption. The Cimel radiometer was on the roof of the Station Marine on 13 June and before 11 h UTC on 14 June; on board Sepia II in the afternoon on 14 June 1994. Although a peak occurred between 13 h UTC and 14 h UTC, very likely due to a cirrus cloud hiding the Sun, the aerosol optical thicknesses were low in the afternoon (around 0.07) on 13 June. The atmosphere was much more turbid on 14 June with a variation ranging from 0.4 to 0.9. 8 July was almost as turbid as 14 June with τ_a around 0.7 in the afternoon. We did not report the results for 5 October, where measurements were collected from the roof; this day was stable and clear with a mean value of τ_a=0.05 at 550 nm.

The Angström exponent a plots (Fig. 5) showed a strong spectral variability on 14 June (a around -1.5). Likewise, such variability was noticed in July (around -1.6). This high exponent points out the occurrence of small particles in the atmosphere. A sensitivity study conducted on the aerosol optical depth shows that the absolute uncertainty $\Delta\tau_a$ is about 0.03 at 550 nm for an air mass value of 1. Thus, in clear sky conditions like those observed on 13 June and on 5 October, the measured optical depth has the same order of magnitude as its uncertainty of determination so that the computation of the absolute Angström exponent is meaningless. Only the relative behavior of a may be used to show up different kinds of particles. On 13 June, it is likely that the strong decrease of a after 17 h (from -0.2 to -1.4) is due to other particles.

Sky Radiance and Degree of Polarization

Sky radiance was collected by REFPOL both on the roof and on the boat in June 1994. The other months, REFPOL was only on the roof where it was settle in the principal plane. Such configuration was not easy to get on board the ship and the scanning planes were multiple. Figure 6 gives examples of set of sky radiance and degree of polarization on 14 June in the principal plane. Since REFPOL gives two values of the radiance at a given scattering angle (one for each side of the sun), we used the zenith angles as x-axis for convenience. The radiance decreases as expected from the blue to the red and near-IR end of the spectrum. On the contrary, the observation of the degree of polarization for this particular sequence is interesting. Usually, the degree of polarization is higher at smaller wavelength because of the larger contribution of the molecular scattering which is highly polarized.

The maximum of the degree of polarization, P_{max}, is located at a scattering angle around 100°. Its behavior is quite continuous and symmetric around this value. We then plotted P_{max} in Figure 7 at 450 nm and 1650 nm for the three above-mentioned days. At 1650 nm, the Rayleigh scattering is negligible, and the polarization is only generated by the aerosols. On 13 June, the degree of polarization increases from 22% to 55% between 4 p.m.

Table 3. Wind (Speed and Direction), Horizontal Visibility, and Relative Humidity

	Wind Speed ($m\ s^{-1}$)	*Visibility (km)*	*Relative Humidity (%)*				
			06 UTC	*09*	*12*	*15*	*18*
13 June 1994	3; N	17	95	83	87	56	57
14 June 1994	2; NW	15–8	86	60	68	78	65
5 October 1994	5; S	55–100	80	73	59	63	65
8 July 1995	6; N	28–8	71	77	72	61	68

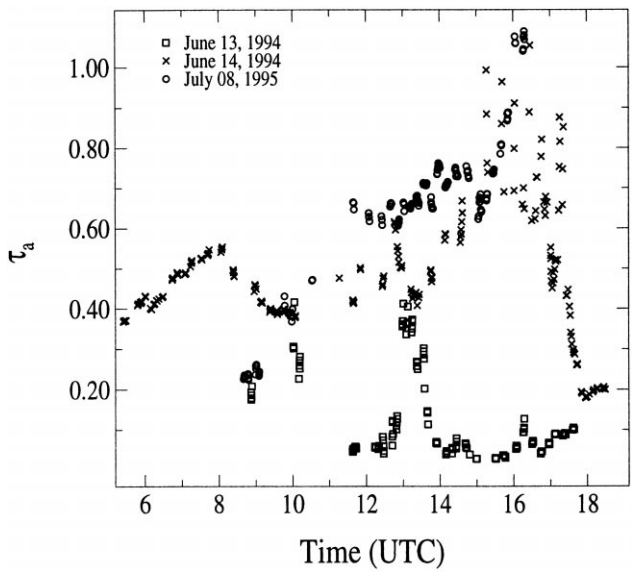

Figure 4. Aerosol optical depth τ_a at 550 nm versus time on 13 June 1994 (□), 14 June 1994 (×), and 8 July 1995 (○).

and 5 p.m. The high value of the maximum degree of polarization at 1650 nm at the end of the afternoon reveals the occurrence of small particles which tend to have a Rayleigh-like polarization. The maximum of the degree of polarization is very sensitive to the Junge slope v; the higher v is in absolute value, the higher this maximum. According to Figure 5, we observe a time variation of a of -1.0. Also, computations with continental aerosols pointed out that such variation of a gives an increase of the degree of polarization of about 25% which is consistent with the measurements (Fig. 7). This maximum is higher in the blue due to a larger contribution of Rayleigh scattering which is quite important during this clear day. Its behavior on 14 June is not common. The maximum of the degree of polarization remains constant and high (almost 65%) at 1650 nm. At the same time, it decreases in the blue with an increasing optical depth at the end of the day as a result of depolarization by multiple scattering. On 8 July 1995, similar features like those described for 14 June 1994 are observed. We notice this day that the degree of polarization decreases with re-

Figure 5. Same as Figure 4 except for the Angström coefficient.

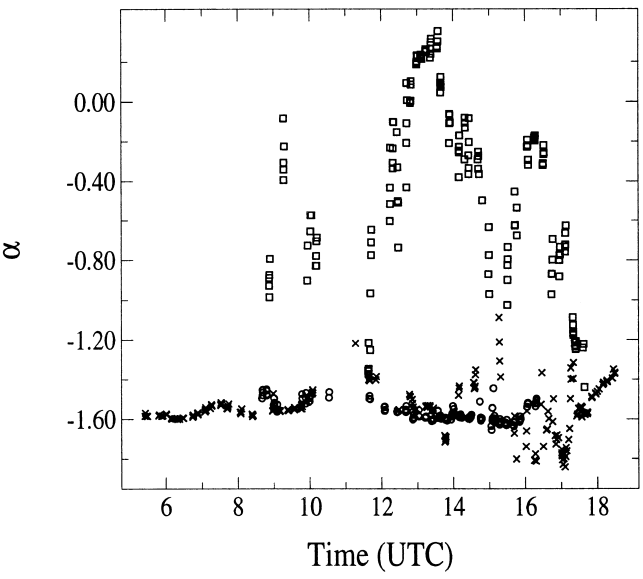

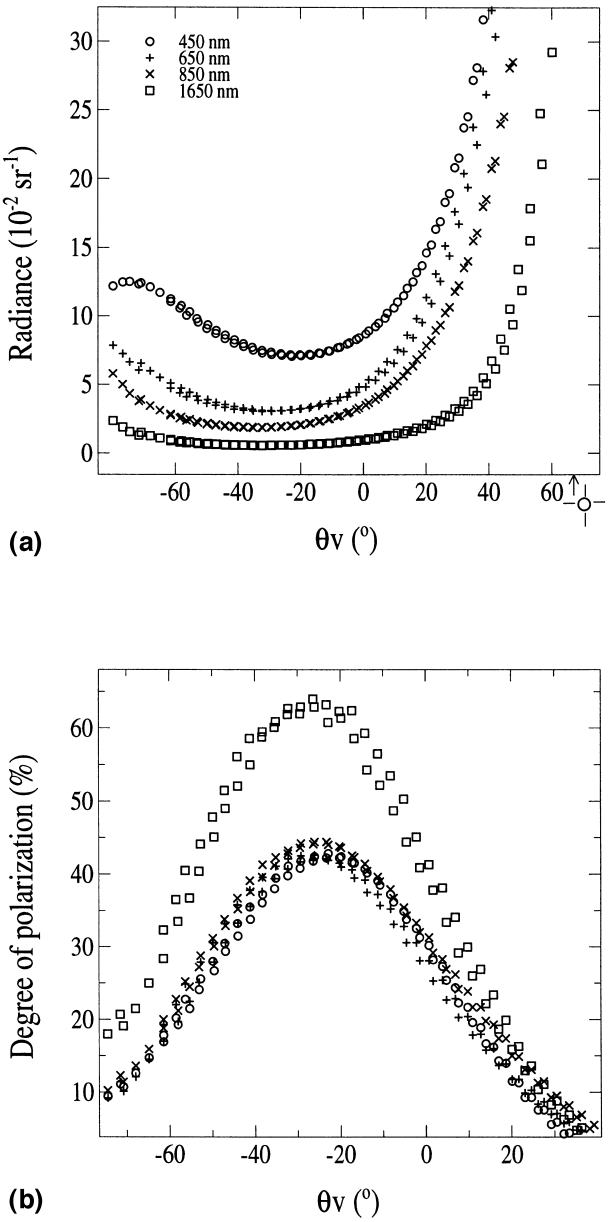

Figure 6. 14 June 1994 at 6 h 9 UT (θ_s=69.8°), atmospheric measurements in the principal plane versus the views angle θ_v. The sun position is specified on the x-axis. a) radiance at 450 nm (○), 650 nm (+), 850 nm (×) and 1650 nm (□); b) degree of polarization (same wavelengths with same symbols).

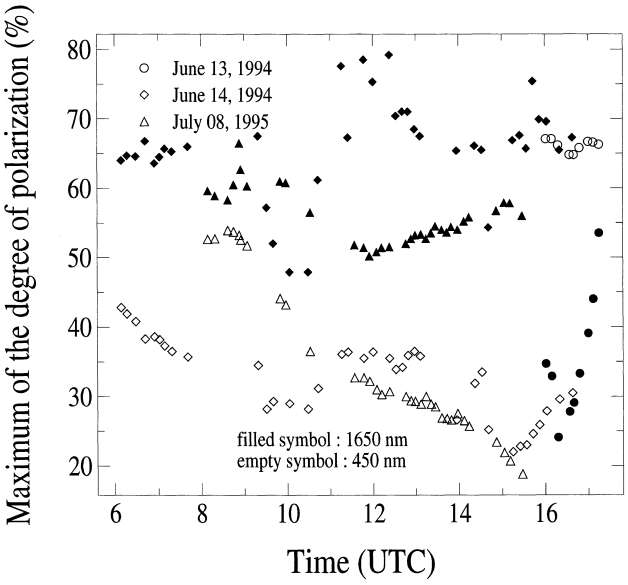

Figure 7. Maximum of the degree of polarization versus time at two wavelengths for 3 days.

spect to the time for each visible wavelength (for instance, at 450 nm, it ranges from 50% on the morning to 20% at the end of the afternoon) whereas it is constant at 1650 nm and around 57%.

This evolution seems to be related to the occurrence of hazes at the site of measurements. We can imagine that a haze developed during the evening of 13 June, according to the process of a cooling of an air mass as described above. This haze would be responsible for the increase of the degree of polarization at 1650 nm and would have persisted up to the end of the day after. It appears on a first step that the particles making up the hazes have a monoscattered mode sensitive in the infrared. In October, although measurements were a little bit noisy at 1650 nm, a behavior of the sky radiance and the degree of polarization similar to 13 June is noted.

POLDER Measurements

For each experiment, POLDER flew along the same trajectory. Two transects along the coastline and a third one across this line were overpassed, but only the inshore–offshore transect, identical to the boat, matters here. Table 4 summaries the different flights over the site. We tried to couple the flights with tide cycles in order to include, in our study, hydrodynamism which is critical in the Straits.

Table 5. SPOT and POLDER Radiances (10^{-2} sr^{-1}) on 5 October 1994

	Central Wavelength		
	550 nm	*650 nm*	*850 nm*
SPOT	10.0	4.7	2.2
POLDER	4.7	2.3	1.1
POLDER+Rayleigh	9.3	4.6	1.9

Considering that POLDER flew at about 2000 m, it is necessary to account for the vertical distribution of the aerosols. Also, the correction for gaseous absorption only concerns the downward pathway. In the case of Rayleigh particles, the scale height usually applied is 8 km while it is 2 km for aerosols. This parameter has to be considered for atmospheric correction. During the experiments, aerosols were very often located below the plane so that the assumption of a scale height of 2 km could be relevant. Moreover, SPOT (Système Pour l'Observation de la Terre) sensor acquired a scene in October. Once we matched geometrical conditions of observations for both SPOT and POLDER images (view angle of 27.6°), we compared radiances at the top of the atmosphere level. The atmospheric absorption was rather low in SPOT spectral bands (550 nm, 650 nm, 850 nm), and we expected satellite radiances to be larger than POLDER ones because of the Rayleigh contribution above POLDER. We then added this component to POLDER measurements and similar radiances to SPOT's were retrieved (Table 5). Given the accuracy of SPOT calibration and atmospheric effects, a good validation of POLDER data by SPOT is observed. It arises also that aerosols may be located in the low layer of the atmosphere and below the plane.

It is reported in Table 6 the instantaneous optical thicknesses measured at POLDER overpass. It is likely that a spatial heterogeneity exists between the land and offshore and is not negligible in this geographical context. So the values have to be adjusted according to the place they were collected.

We give Figure 8 as an example of POLDER measurement at 870 nm in June and October 1994. Since the water leaving radiance is negligible at this wavelength off the coast, the signal is mainly attributed to the

Table 4. POLDER Flights and Tides Conditions[a]

	13 Jun 94	*14 Jun 94*	*5 Oct 94*	*8 Jul 95*
Time (UTC)	14 h 30	08 h 43	11 h 02	13 h 29
θ_s, φ_s(°)	41.4, 243.5	46.0, 108.7	55.8, 168.4	33.3, 220.2
Low tide (UTC)	8 h 25	9 h 3	18 h 08	13 h 34
High tide (UTC)	13 h 31	14 h 11	10 h 40	6 h 12

[a] θ_s and φ_s are respectively zenith and azimuth solar angles.

Table 6. Aerosol Optical Thickness at POLDER Overpass

	13 Jun 94	*14 Jun 94*	*5 Oct 94*	*8 Jul 95*
τ_a (440 nm)	0.070	0.607	0.052	0.947
τ_a (670 nm)	0.057	0.322	0.020	0.483
τ_a (870 nm)	0.069	0.207	0.014	0.319

atmospheric component. In the primary scattering approximation, we have Eq. (1):

$$L=\frac{\tau p(\theta)}{4\mu_v}, \tag{1}$$

where $p(\theta)$ is phase function for the molecules and aerosols mixture, τ the total optical thickness, θ the scattering angle, and μ_v the cosine of the view zenith angle. After correction for the air mass applied to the whole image, except the sunglint spot, we get a quantity function of the optical thickness and of the phase function.

To cancel any water reflectance contribution in red and near-infrared, we first selected POLDER images as far as we could from the coast. Moreover, we verified that water bodies concerned for offshore scenes belong to Case I waters. Measurements carried out on the water column revealed a chlorophyll and suspended matter concentration, respectively, below 2 mg/m^3 and 1 mg/L for off-sampling stations. Also, REFPOL scans above the sea surface pointed out water leaving radiance at 650 nm around 0.2×10^{-2} sr^{-1} on 14 June 1994 (Fig. 9) while POLDER signal, on the same zone, is about 10 times larger. The water bodies effects are then negligible.

The comparison, Figure 8, with the pure molecular case gives clues about the turbidty of the atmosphere. This plot illustrates two different conditions with a clear sky in October which contrasted with an intense particle concentration in June. Nevertheless, a strong variation of the radiance occurred at a given scattering angle on POLDER measurements. We first thought that it was due to instrumental noise. We then smoothed the images averaging successively on a 4×4, 8×8, and 16×16 pixel zone. Any instrumental noise should be significantly reduced as the pixel area increases. We added in Figure 8 the radiance smoothed using a 4×4 pixel area, and we noticed that its variation, at a given scattering angle, is independent of the width of the average pixel zone. The assumption of a possible instrumental noise is questionable. We also studied the local variabilities of the pixels within 16×16 areas. We then computed the ratio $(\rho_{max}-\rho_{min})/(\rho_{max}+\rho_{min})$ in those areas at 870 nm and 670 nm (Fig. 10). The variability is a few percent only. Its spectrally flat aspect suggests that it is not related to ocean color effects which may be more significant at 670 nm. Thus, the dispersion seems to be related to small local variations of aerosols.

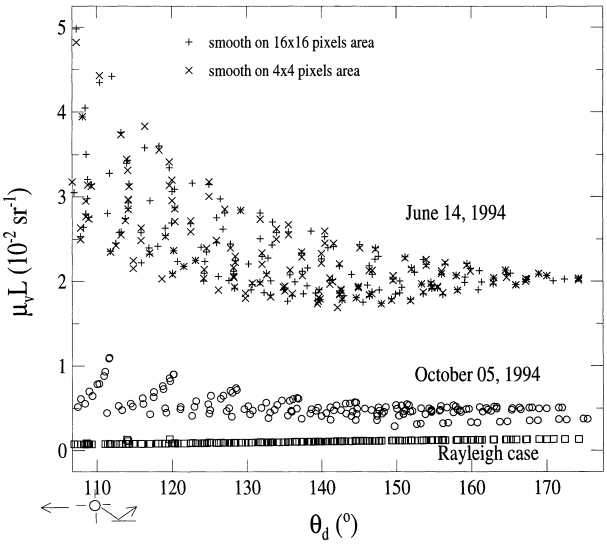

Figure 8. POLDER radiances (in 10^{-2} sr^{-1}) at 870 nm (after correction of the air mass μ_v). These values are plotted versus the scattering angle for a theoretical molecular atmosphere, for the clear day on 5 October 1994 and for 14 June 1994. A smoothing applied for two different pixel zones (16×16 and 4×4) is also shown for 14 June 1994. The direct sunglint position is specified on the *x*-axis.

A pattern regularly appeared around the sunglint spot when the scattering angle ranged from 110° to 125° (Fig. 8). We investigated a possible geometrical effect, and we computed, for the C70 SF model, the quantity μ_v L with respect to the azimuth angle. Figure 11 illustrates the results of these computations once the scattering angle was set up i) to 110° and ii) to 120°. We first tuned at τ_a=0.400 at 870 nm in order to retrieve the observed radiance. The Fresnel reflection was included,

Figure 9. Water leaving radiance at 670 nm above the sea surface (REFPOL) and at plane level (POLDER).

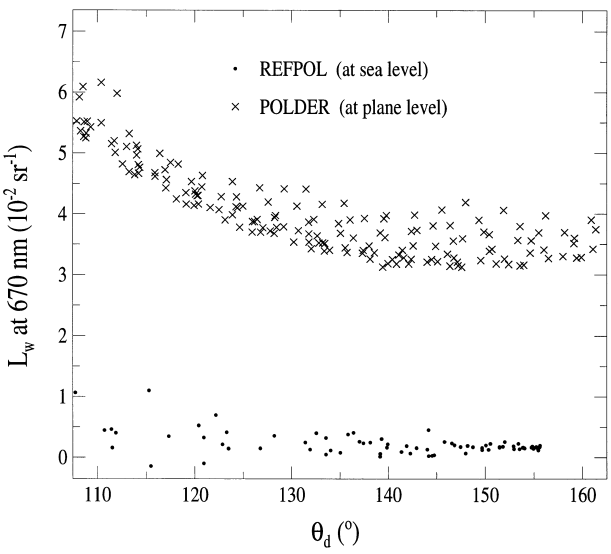

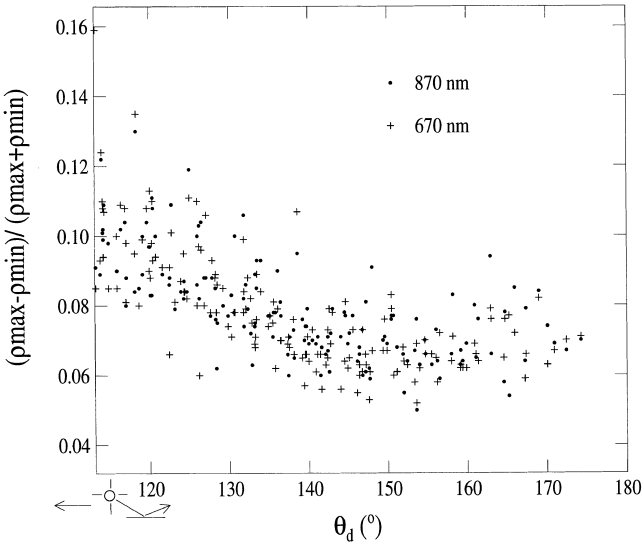

Figure 10. Relative variation at two wavelengths $(\rho_{max}-\rho_{min})/(\rho_{max}+\rho_{min})$ of the radiance within a 16×16 area on 14 June 1994 on POLDER data.

which means that we accounted for the direct sunglint and for the ocean–atmosphere coupling (sky reflection on the water) in the computations. The shape obtained in Figure 11 is very similar to the observed patterns (Fig. 8) so that they could be attributed to a geometrical effect (especially the azimuth). The azimuth dependence of the Fresnel reflection clearly appeared here as expected. It was more pronounced for a scattering angle of 110° rather than 120°. At 110°, we were outside of the direct sunglint spot, and the coupling effects dominated. At 120°, we moved again outside of the direct sunglint spot, and the coupling effects were lesser so that the azimuth dependence decreased. For the other days of measurements, the direct sunglint spot occurred on POLDER scenes for scattering angles ranging from 90° to 110° (see Fig. 2); the ocean–atmosphere coupling effects could be important up to 125°. They were more or less pronounced between 110° and 125° according to the solar elevation during the POLDER acquisitions.

Figure 11. Azimuthal dependence of μL for C70 model. We looped on τ_a to retrieve the radiance level of POLDER data (τ_a=0.400 at 870 nm on 14 June 1994). Two scattering angles are shown (110° and 120°). The case with no Fresnel reflection is also illustrated at 110°.

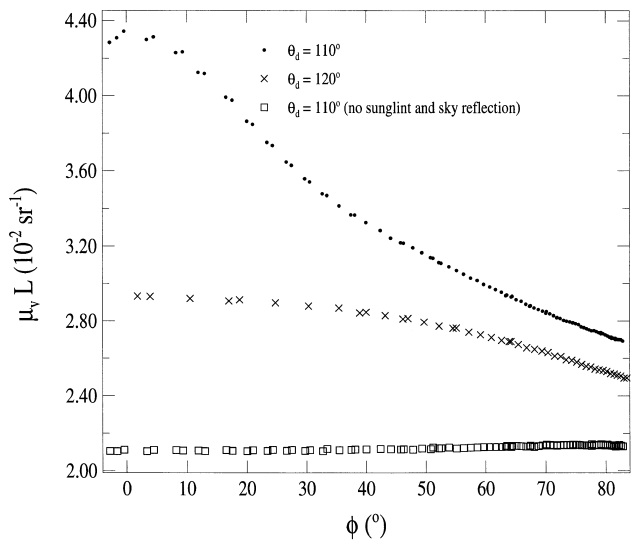

Also, we studied the impact of the multiple scattering in the atmosphere removing the Fresnel reflection (squared symbol in Fig. 11). This time, there were no significant effects of the azimuth and the multiple scattering played no role in the dispersion of data as it appears in Figure 8. In a more sophisticated analysis, we need to include the Fresnel reflection.

ANALYSIS AND DISCUSSION

Sky Radiance—Degree of Polarization

The successive order of scattering method (Deuzé et al., 1989) was used as the radiative transfer code to compute the downwelling radiance at sea level. This code does not include gaseous absorption, which can be dissociated from scattering processes. The main inputs to the code are the Rayleigh optical thickness (standard value at sea level), the measured aerosol optical thickness, and the aerosol model. A first crude description of the aerosol model consists in using the Junge power law as a size distribution for aerosols (Junge, 1952) with a slope $v=a-3$; the refractive index m remains to be determined.

Since the atmosphere was clear in October and the degree of polarization behaved classically, it would be relevant to think that a Junge law is suitable. We considered first in our model a refractive index of continental particles $m=1.50-0.001j$ with an Angström exponent $a=-1$ typical for this model and consistent within the error bars with the measured one. Because the accuracy of the aerosol optical thickness derived from solar extinction measurements is poor in relative value, we adjusted this parameter in order to retrieve the measured radiance. Figure 12 illustrates this retrieval and shows that the degree of polarization is also quite well retrieved in October with the continental aerosol model. On 13 June (Fig. 13), the REFPOL data were also retrieved (with more difficulties for the polarization) by this continental aerosol model. On a more semiquantitative basis, in the late afternoon of 13 June, the increase of P_{max} at 1650 nm from 20% to 55% (see Fig. 7) was correlated to the decrease of a between −0.8 and −1.6. Computations with a Junge law and $m=1.50$ indicate that, for this variation in a, the degree of polarization increases from 20% to 50% which closely corresponds to the measurements reported in Figures 3 and 5. Within a few hours, another

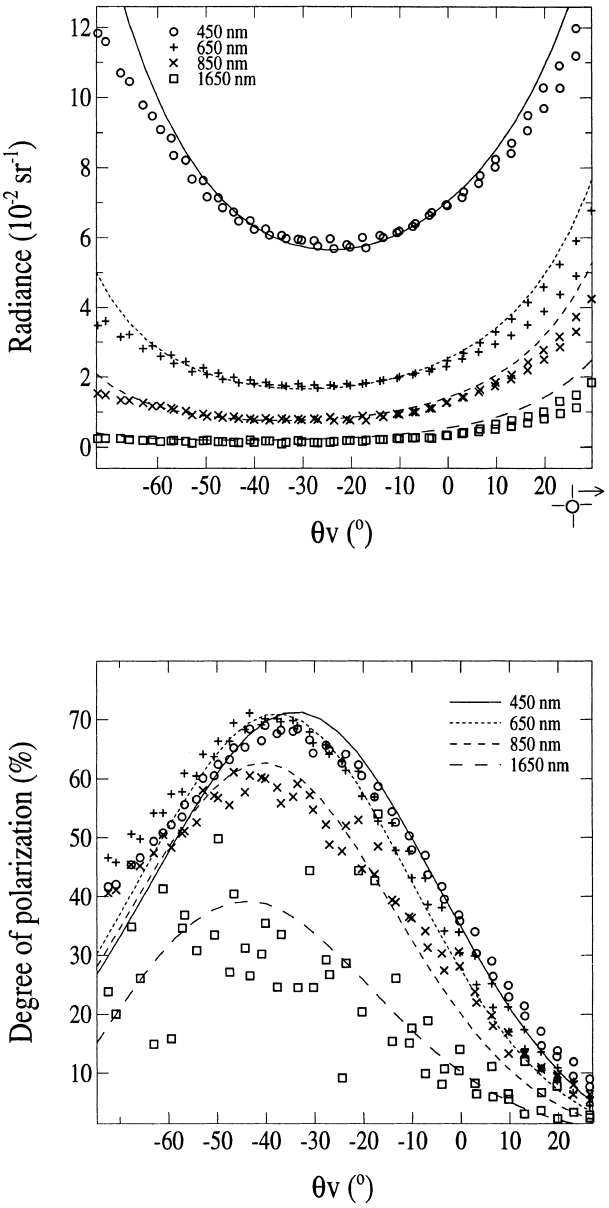

Figure 12. Retrieval of the sky radiance and polarization measurements as measured on 5 October 1994 in the principal plane (θ_s=56°) by REFPOL. Labels for the wavelengths used are indicated in the upper graph. The measurements are retrieved with a Junge size distribution law which parameters are: a slope $v=-4$, a refractive index $m=1.50-0.001j$ and an aerosol optical thickness equal to 0.06 at 550 nm. Symbols are used for measurements and solid lines for model predictions.

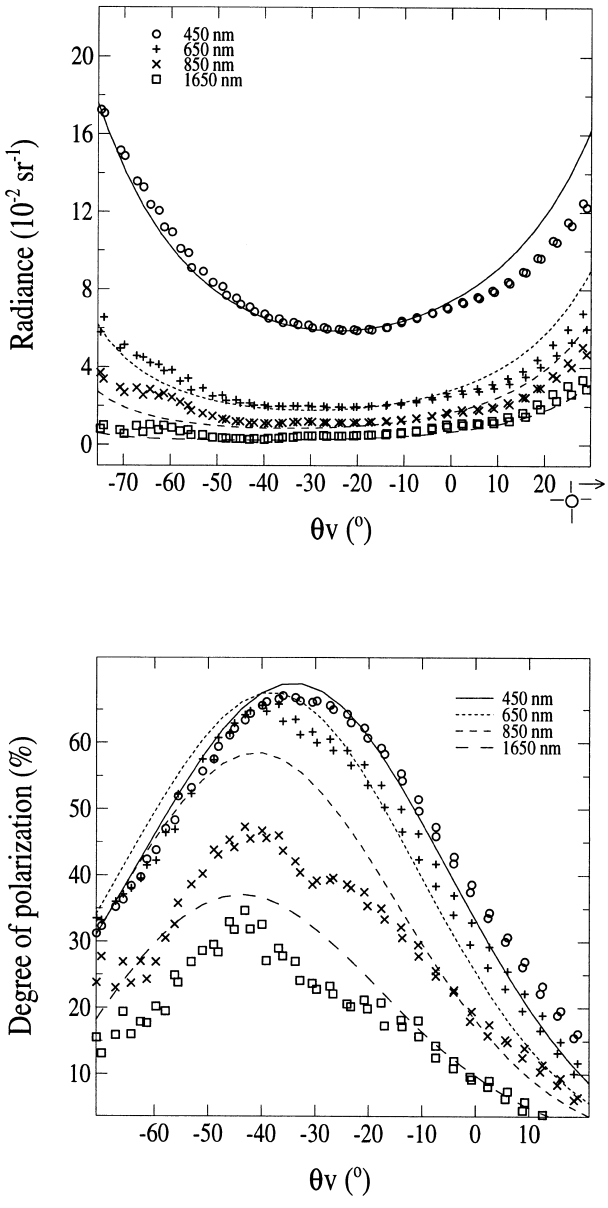

Figure 13. Same as Figure 12 for 13 June 1994 (θ_s= 54.5°). The Junge law has the following parameters: $m=1.50-0.001j$, $v=-4$, and $\tau_a=0.075$ at 550 nm.

kind of particle appeared which seemed still to be described by a power law.

Early in the morning of 14 June 1994, the aerosol optical thickness was quite large (Fig. 4). In Figure 7, P_{max} at 1650 nm is almost identical to the last measurement of 13 June. But P_{max} in the blue is lower. The same remark applies for 8 July 1995. For a power law, the phase matrix is spectrally independent; it is then foreseen that the polarization will be larger at small wavelengths because of the additional contribution of the Rayleigh. We also tried unsuccessfully to retrieve the 14 June measurements using the gamma standard law shown in Eq. (2):

$$n(r)=r^{(1-3v)/v}e^{-r/v\bar{r}}, \tag{2}$$

where $\bar{r}$ is the effective radius and v the effective variance. We scanned for different refractive indexes ranging from 1.33 to 1.55, for radii ranging from 0.1 μm to 0.6 μm, and for variances ranging from 0.1 to 0.6. A same attempt to retrieve the measurements using a log-normal size distribution also failed.

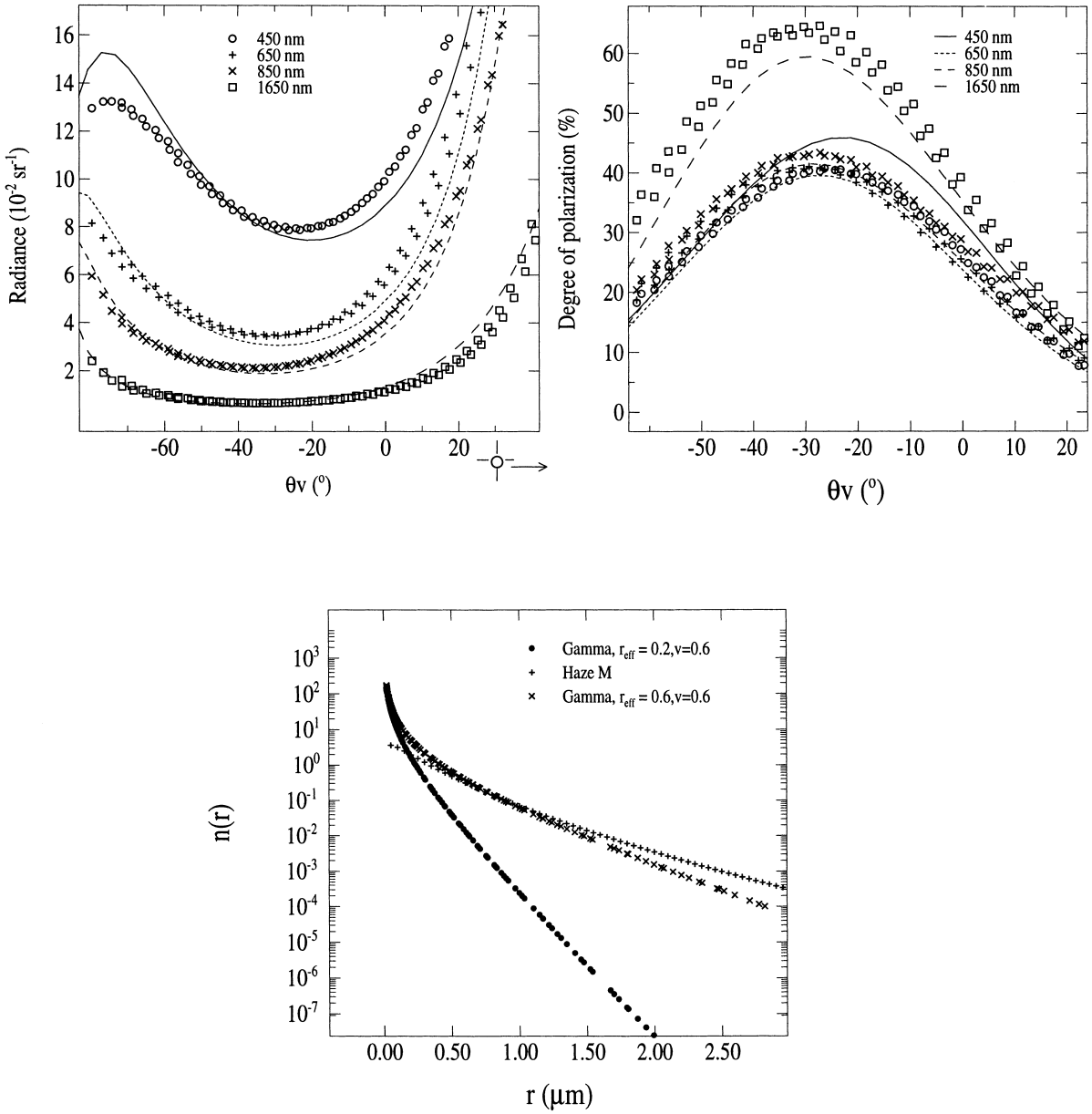

Figure 14. Same as Figure 12 for 14 June 1994 (θ_s=66.5°). A mixing of two size distributions enables to retrieve the data: i) a Junge size distribution with $v=-4$, $m=1.50-0.001j$, and $\tau_a=0.073$ at 550 nm; ii) a Gamma standard size distribution with $m=1.40-0.001j$, $r_{eff}=0.2$ μm, $v_{eff}=0.6$, and $\tau_a=0.253$. Gamma laws for two effective radii ($r_{eff}=0.2$ μm and 0.6 μm) are also shown and compared with Haze M size distributions.

It is expected here that hazes are going to complicate measurement retrieval. Two successive days of data are available in June 1994. The first set of measurements we acquired on 13 June (16 h 1 UTC) corresponded to a Junge law prediction and this data set represents the background aerosol. A thorough analysis consists in adding another mode of particles to the Junge one. With this objective, we introduced a gamma standard law. This size distribution is convenient because it has two adjustable parameters helpful in determining this unknown mode accurately. In order to determine the second mode responsible for the high degree of polarization at 1650 nm on 14 June, we subtracted, given a geometry, aerosol present in the atmosphere on 13 June, which obey to a Junge law distribution, from the measurements collected on 14 June. We tried then to retrieve the remaining with the gamma standard law, looping on r, v, and m. The best fit showed up a submicrometric mode of particles ($\bar{r}=0.2$ μm and $v=0.6$) whose size distribution is plotted in Figure 14. We compared with another Gamma law ($\bar{r}=0.6$ μm, $v=0.6$) and a haze M distribution. The value of 1.40 as real part of the refractive index suggests the maritime nature of the particles. The effective radius ($\bar{r}=0.2$ μm) is rather low. An increasing radius gets

Table 7. Comparison of Angström Exponent with Spectral Variation of Aerosol Reflectance for Shettle and Fenn Coastal Models[a]

	C70	*C90*	*C98*
a	0.65	0.42	0.28
$\varepsilon'=\log(\varepsilon)/\log(\lambda_i/\lambda_j)$	0.75	0.48	0.36

[a] ε' is computed between 870 nm and 670 nm considering a mean value of ε.

closer to a haze M distribution, typical of maritime hazes; we can assume that the small particles correspond to Aitken nuclei, which sizes are usually below 1 μm, expressing a haze growing up. This explanation would be consistent with the time of the data set, early on the morning (6 h 9 UTC). Figure 14 also shows the combination of both Junge and gamma law; a good retrieval of the REFPOL measurements is obtained.

Likewise, the same approach for 8 July was conducted, and a mixing of aerosol size distribution was made. The best model that fits the data is as follows:

$m=1.45-0.001j, \quad \upsilon=-4.5, \quad \tau_a=0.063$

at 650 nm for Junge law,

$m=1.38-0.005j, \quad \bar{r}=0.3\mu\text{m}, \quad \upsilon=0.6, \quad \tau_a=0.500$

at 650 nm for gamma law.

An accurate description of the aerosols was derived from the measurements. This stage enables us to figure out their local climatology. It is then possible to think about atmospheric correction on POLDER images provided that optical thickness is adjusted because of the spatial variability of aerosols.

Spectral Variation of Aerosol Radiance

Since the Gordon coefficient is a key parameter in the atmospheric correction scheme (see the Introduction), it is interesting to study its behavior regarding our measurements. This coefficient is derived by correcting for our data of gaseous transmittance. We predicted the radiance for a Rayleigh atmosphere and then substracted it from the original signal, for an identical geometry, to get the aerosol radiance. This method does not remove the multiple scattering effects (while Gordon does), but it will be applied systematically for theoretical results as well as for truth data. ε features may help to identify aerosol model. Mathematically, it is defined by Eq. (3):

$$\varepsilon=(\rho_a(\lambda_i)/\rho_a(\lambda_j)), \tag{3}$$

where ρ_a is the aerosol reflectance. As well, to compare to a, we define ε' in Eq. (4):

$$\varepsilon'=\frac{\log\varepsilon}{\log(\lambda_i/\lambda_j)}. \tag{4}$$

The Junge power law shows that it is slightly dependent of the scattering angle and is closely related to Angström exponent a. The particle phase function is then independent of wavelength when a large size spectrum is considered. Some of Shettle and Fenn's models, like coastal models, also have this property (Table 7) with a flat angular behavior of ε except in backward and forward scattering.

In order to compare the Angström exponent, we computed ε' between 850 nm and 650 nm for REFPOL sky radiance as a function of view angle. Illustrations are given in Figure 15 for several sets of measurements. The angular variation observed is always significant. For instance, in July 1995, the values range from -0.8 to -2.0. ε' is then different from a. A Junge law size distribution is not relevant in this case, and this confirms the previous results. At first glance, the strong angular variation of ε' suggests that the SF models are not suitable to describe the actual aerosols. This conclusion was also drawn by Chami et al. (1995), from the strong angular dependence of ε' in the POLDER data.

Because the SF models are very popular in the atmospheric correction algorithms for ocean color sensors (for example, for the SeaWiFS algorithm, see Gordon and Wang, 1994), and despite the first conclusion drawn above, we tested these models for the REFPOL measurements retrieval. For example, the T90 model appears suitable on 14 June (Fig. 16a) with an optical depth $\tau_a=0.232$ at 850 nm. The spectral variation of the tropospheric models T is the strongest among the others (M and C) and the closest to those measured by REFPOL in the backscattering direction. The ε' coefficient is well bounded by the T98 and T90 models, except in the forward direction certainly because of the large diffraction peak of the continental model. The measured radiances are well retrieved by the T90 model if we ignore the forward scattering (Fig. 16b), as well as we can retrieve (Fig. 16c), the large degree of polarization observed at 1650 nm. The different kinds of particles suggested in the SF models appeared reliable to describe situations as complex as for this day. For 8 July 1995, the selection of an SF model based on ε' was more challenging because of the large angular variations derived from REFPOL (Fig. 15). Nevertheless, using the T98 model, the radiances are quite well retrieved except in the forward scattering; the computed degree of polarization at 1650 nm is simply too high. Table 8 lists the SF models used to retrieve REFPOL data with the corresponding optical depth.

We also tried to select one of the SF models based on ε' determination. The multiangular observations of a POLDER scene were first corrected for the Rayleigh as follows: We simulated a POLDER image for a pure molecular case. The direct sunglint spot was accounted for as well as the ocean–atmosphere coupling effects (sky reflection at the sea surface). Then we subtracted this image to the POLDER truth measurements which accounts of the total sunglint (direct+coupling). This method is

approximate if we consider the direct sunglint spot; this is the reason that we do not work on this zone and we applied a sunglint mask. After these corrections, we get ε'. For example, on 14 June 1994, an histogram in ε' indicated a mean value of -1 but with a dispersion at half width of 0.22. The computed images for the SF models are much more homogeneous in ε'; always for 14 June 1994, the histogram was peaked for model T98 at -1.22 with a half bandwidth of only 0.2. Figure 17 illustrates the large variations in ε' as observed on the images. It is difficult to conclude about the meaning of such variation in October since optical thicknesses are very low. On 8 July 1995, we noticed that the ε' parameter shows a strong variability with scattering angle of the same order of magnitude as sky measurements. We retrieved in Figure 17 the previous observation made for Figure 8, which is related to the strong variation of ε' at a given scattering angle for POLDER data. The comparison between measurements and theoretical predictions of ε', in this figure, is consistent, which means we account for the Rayleigh–aerosol coupling for both kinds of data. This suggests that multiple scattering effects could not be responsible for the observed variation since model results are homogeneous at a given angle (optical depth and single scattering case do not play a role in the computation of ε' as illustrates the sensitivity of ε' in Fig. 17). We check here the conclusions drawn for POLDER radiance (Fig. 8), and we can attribute the variations to aerosols.

Two sensitivity studies were conducted on ε'. The first one expresses the systematic bias occuring on each pixel accounting for the interband errors. The POLDER absolute radiometric accuracy was assumed to be 5% for

Figure 15. Spectral variation of the aerosol reflectance between 650 nm and 850 nm, versus the view angle, as derived from the REFPOL measurements in the principal plane (the Sun is located in the plane $\theta_v > 0$).

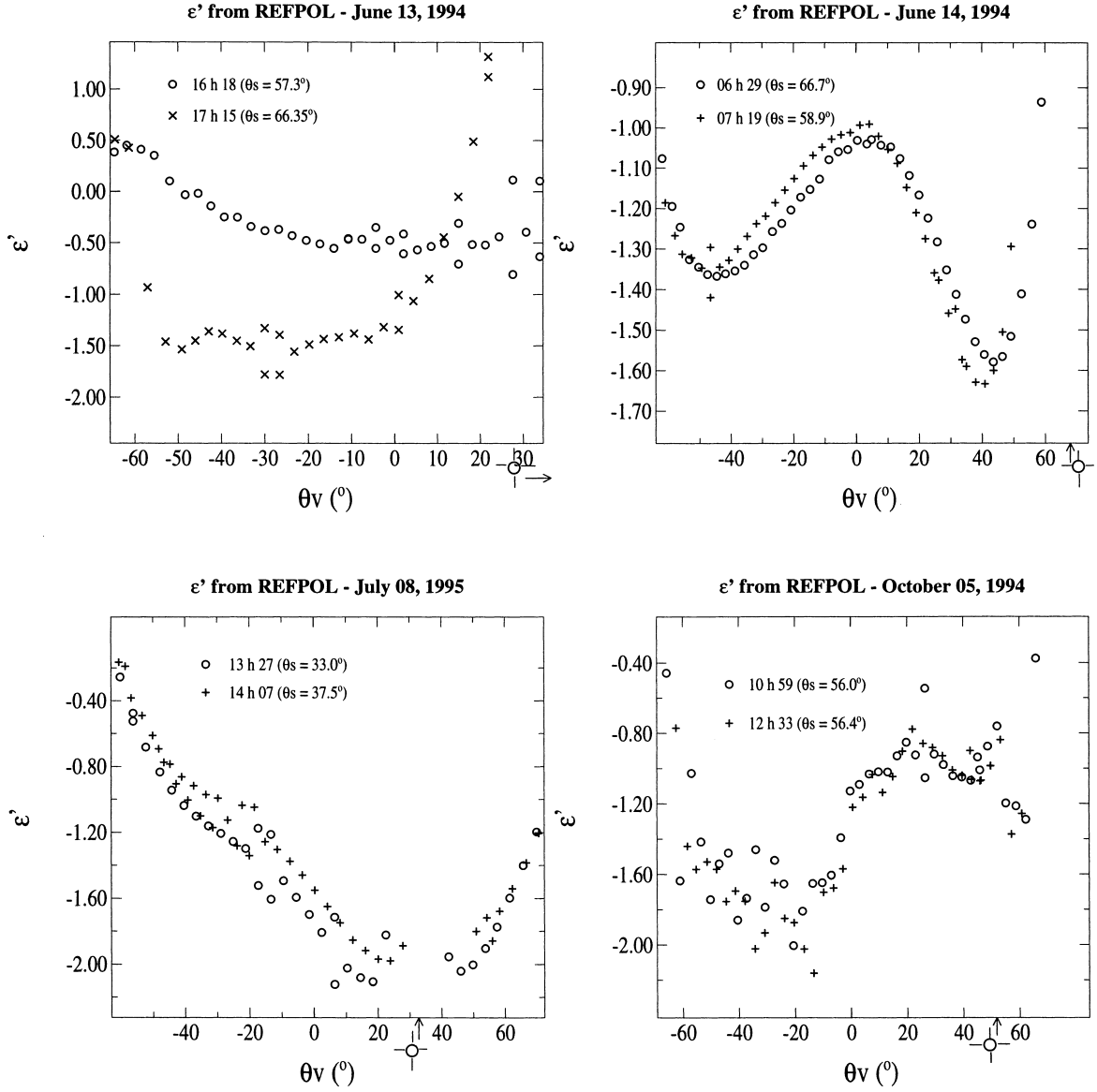

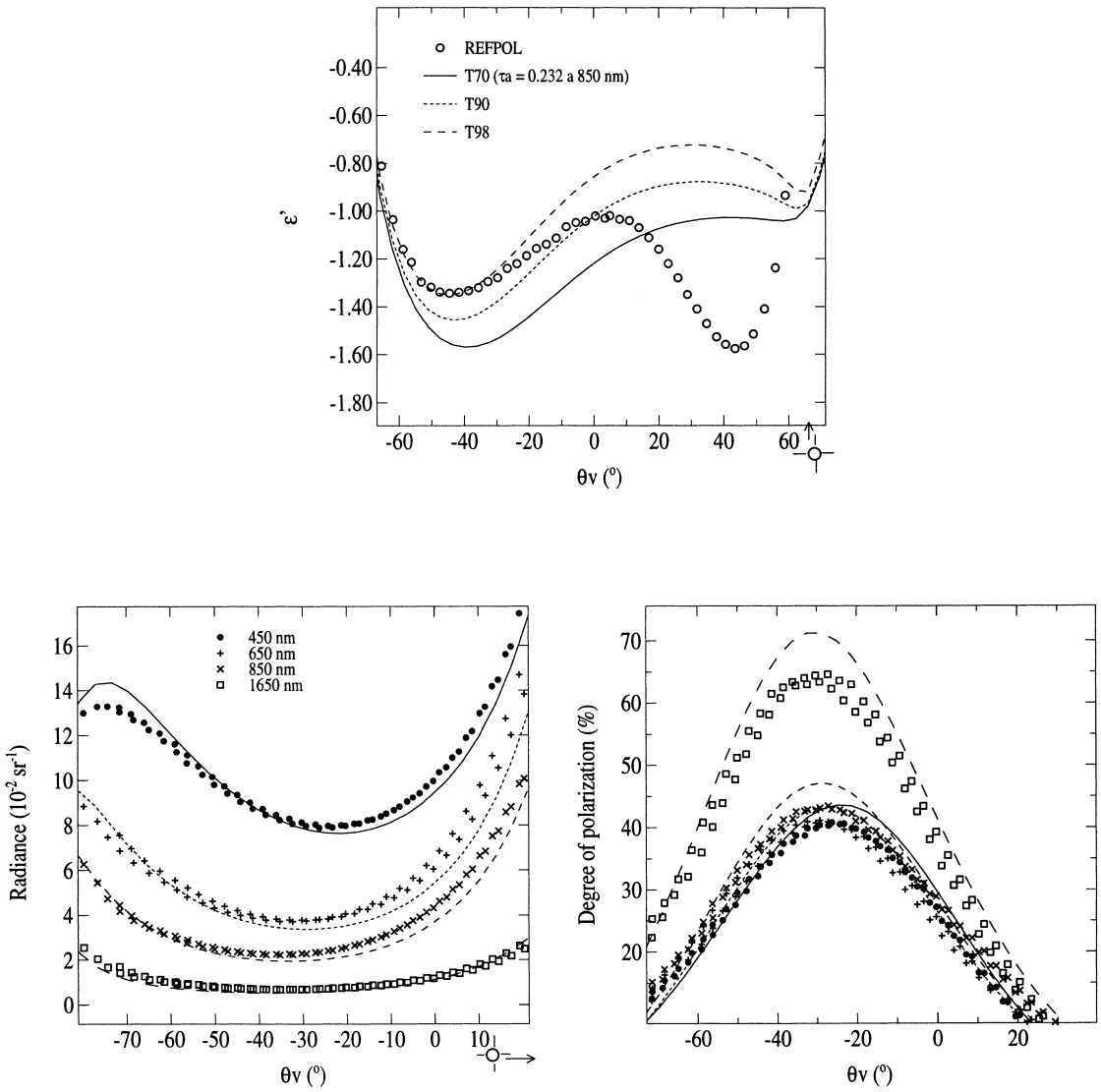

Figure 16. Analysis of the REFPOL measurements on 14 June 1994: a) identification of the SF model based on ε' retrieval (T90, τ_a=0.232 at 850 nm); b) restitution of the REFPOL radiances; c) restitution of the REFPOL degree of polarization.

the absolute calibration at 670 nm and 3% interband calibration between 670 nm and 870 nm. This study showed that ε' is known with an absolute uncertainty $\Delta\varepsilon' = \pm 0.10$ when τ_a=0.5 at 870 m (i.e., for 14 June 1994 and 8 July 1995) and ± 0.3 for 5 October 1994 and 13 June 1994. This error affects ε' in the same way over all the image. The analysis also indicated the weak dependence of this error on the geometry. The large angular variations of measured ε' are then certainly representative of discrepancies between the SF models and the actual one.

Table 8. Shettle and Fenn's Models Used to Retrieve REFPOL Measurements in Sky Radiance and Degree of Polarization

	13 Jun 94	*14 Jun 94*	*5 Oct 94*	*8 Jul 95*
Model	M70	T90	C70	T98
τ_a (at 870 nm)	0.10	0.232	0.05	0.400

The second analysis was focused on the interpixel variation. Figure 8 illustrated that instrumental noise was not responsible for the dispersion of the radiance at a given scattering angle. The dispersion of ε' as it appears in Figure 17 for the POLDER images results from statistical errors. We computed $\Delta\varepsilon'$ in Eq. (5), through Eq. (5), in order to assess the errors induced by the local variations of the pixels.

$$\Delta\varepsilon' = \Delta(\log \varepsilon) = \left(\frac{(\rho_{\max} - \rho_{\min})}{\rho_a}\right)_{\lambda=670\text{ nm}} + \left(\frac{(\rho_{\max} - \rho_{\min})}{\rho_a}\right)_{\lambda=870\text{ nm}}. \quad (5)$$

Results are reported in Figure 18 for 14 June 1994. $\Delta\varepsilon'$ is about 0.3 in the backscattering region, and this value is consistent with the variation observed in Figure 17. A variability of the aerosols occurs. It is at the same

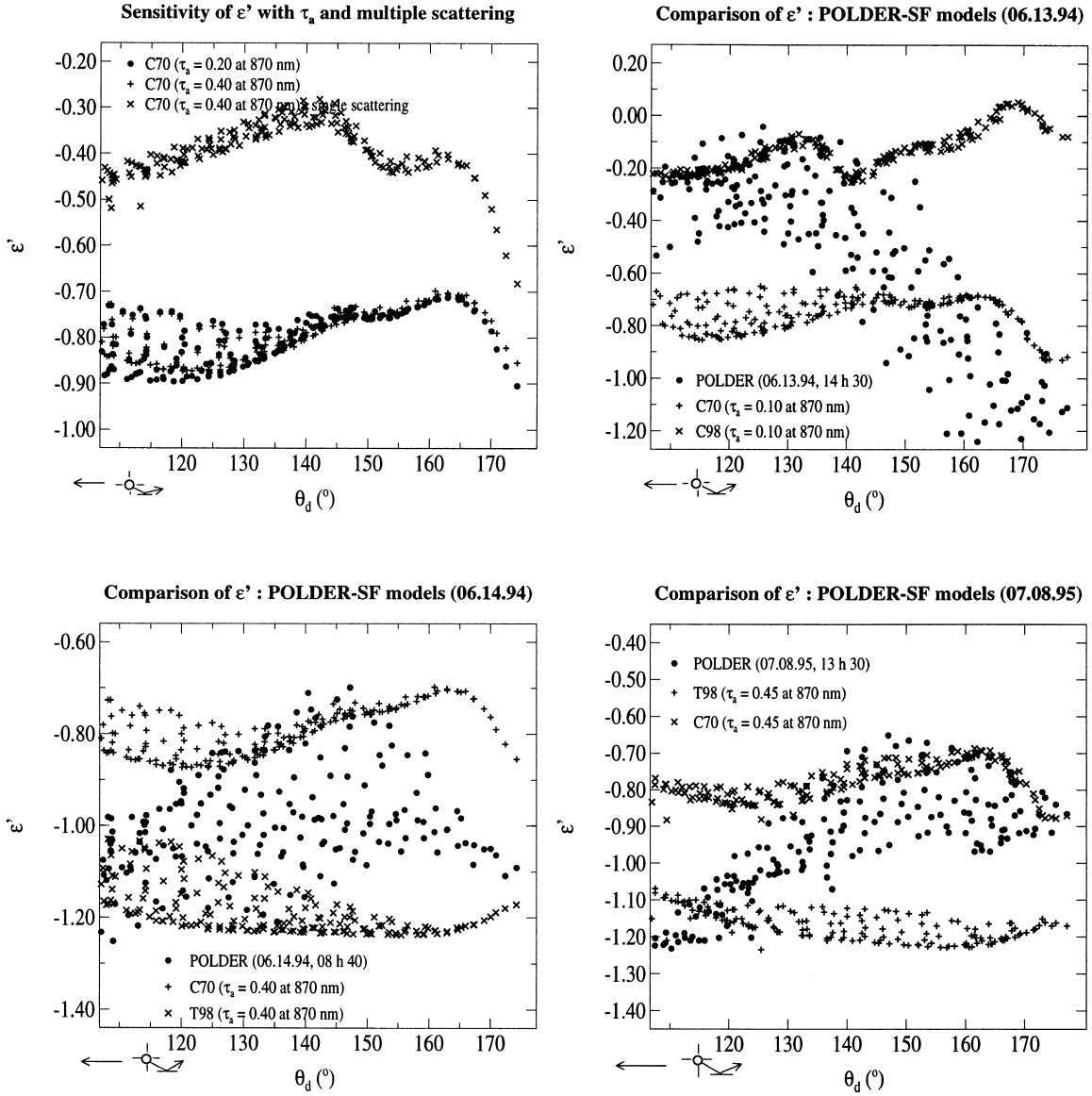

Figure 17. Gordon coefficient ε' as derived from the POLDER images at different dates. ε' is plotted versus the scattering angle after applying a sunglint mask. Sensitivity of ε' with optical depth and multiple scattering is also illustrated (single scattering means primary scattering).

time high enough to be responsible for a strong variation of ε' and still low enough (only a few percent) to be noticeable on REFPOL data sets.

Also, we mentioned previously that geometrical effects upon azimuths occur especially around the sunglint spot. The computation of ε' for C70 model with respect to azimuth or zenith angle at a given scattering angle (θ_d=110°) shows a variation $\Delta\varepsilon' = \pm 0.1$. So, a local variability of the aerosols coupled to geometrical effects seem to explain the dispersion of ε' at a given scattering angle.

Generally, if we want to select one SF model based on ε', we suggest using an averaged value on the image. Table 9 reports the SF models used for POLDER atmospheric corrections.

Comparison between REFPOL and POLDER Aerosol Models

The direct comparison between REFPOL and POLDER radiances is difficult because the range of scattering angle does not match except around 110°, which corresponds to the sunglint spot on POLDER scenes.

The aerosol models retrieved for each sensor are summarized in Tables 8 and 10. When the atmosphere is turbid (i.e., on 14 June and on 8 July), the signature of small particles is visible on the degree of polarization measured by REFPOL as well as on the tropospheric aerosol models derived from POLDER data which have the highest spectral variation among the others. The growth of hazes should explain such aerosols. The clear-

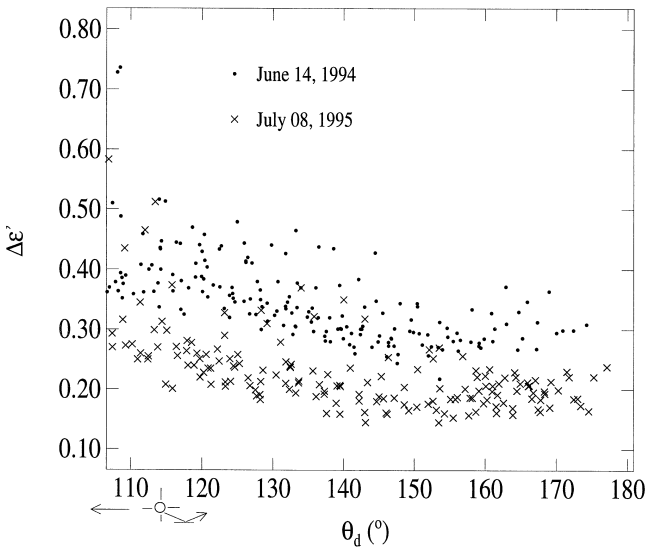

Figure 18. Error $\Delta\varepsilon'$, calculated with Eq. (5), within 16×16 areas on POLDER data on 14 June 1994 and on 8 July 1995.

est days are well described by coastal aerosol models both on REFPOL and POLDER data suggesting larger particles coming from the continent. The aerosol optical depth derived from the measurements highly differs between the two instruments. REFPOL values are consistent with the instantaneous measurements (Table 6). Optical thickness derived from POLDER scenes departs from those derived from REFPOL scans by almost a factor of 2 especially on 14 June. The correspondence between REFPOL and the Cimel radiometer could be explained since these radiometers were set up at the same place (on the roof of the laboratory). On the contrary, POLDER acquisitions occurred offshore at 20 km far from the coastline. An offshore haze of about 70 m height could induce spatial aerosol inhomogeneities hardly visible on REFPOL data. It would explain the discrepancy in the aerosol optical depth retrieval.

Also, since the SF models used for POLDER and REFPOL data rigorously differ (Tables 8 and 9), we compared their own properties. To this end we computed the atmospheric functions (atmospheric radiance and total transmittance at TOA) of each model. An illustration of the results is shown in Figure 19 for 13 June 1994. A good agreement is obtained while the maritime and coastal models are respectively used for REFPOL and POLDER. The same comparison carried out on 14 June 1994 with similar results, provided that optical depth is adjusted for SF model used on REFPOL (τ_a=0.34 at 870 nm instead of 0.232). On 8 July 1995, SF models are quite the same for both instruments (close to T98) so that a consistency is easily obtained. We showed throughout this study that common properties are observed between the SF models retrieved from REFPOL and POLDER. These properties (atmospheric functions) are the parameters we need to proceed to atmospheric

Table 9. Models Used for Atmospheric Correction of POLDER Images[a]

5 October 94	C70; τ_a=0.10
3 June 94	C70, C98; τ_a=0.10
14 June 94	T98, C70; τ_a=0.400
8 July 95	98, C70; τ_a=0.450

[a] τ_a is given at 870 nm.

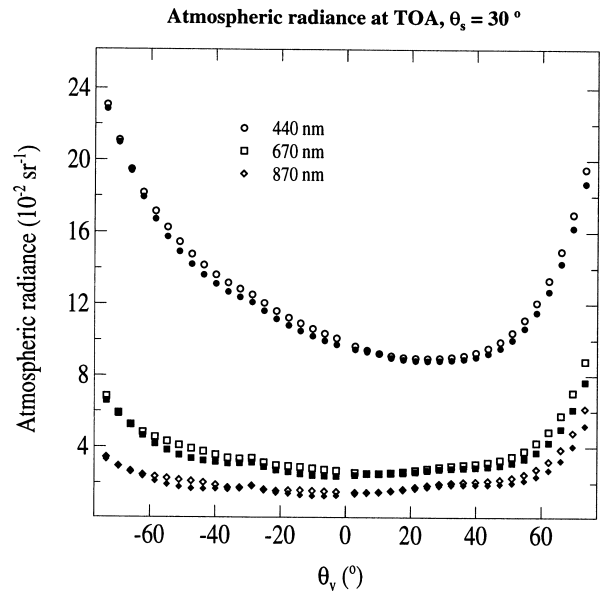

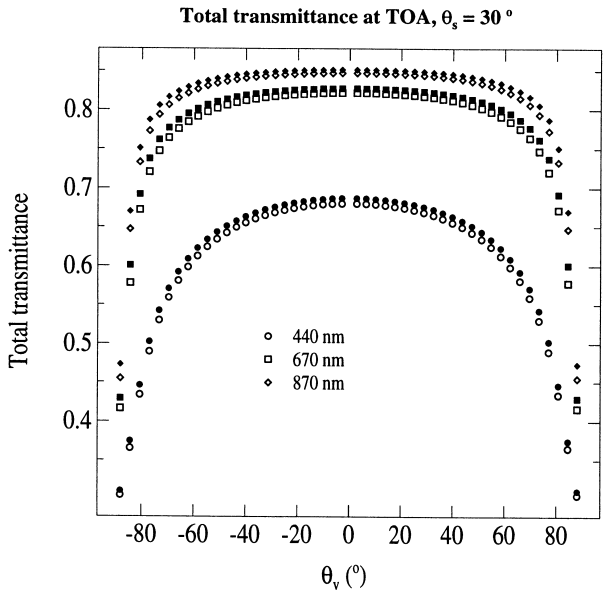

Figure 19. Atmospheric functions (radiance and total transmittance) computed for SF models used on REFPOL (M70, τ_a=0.100 at 870 nm) (clear symbols) and POLDER (C98–C70, τ_a=0.100 at 870 nm) (filled symbols) data on 13 June 1994 (θ_s=30°).

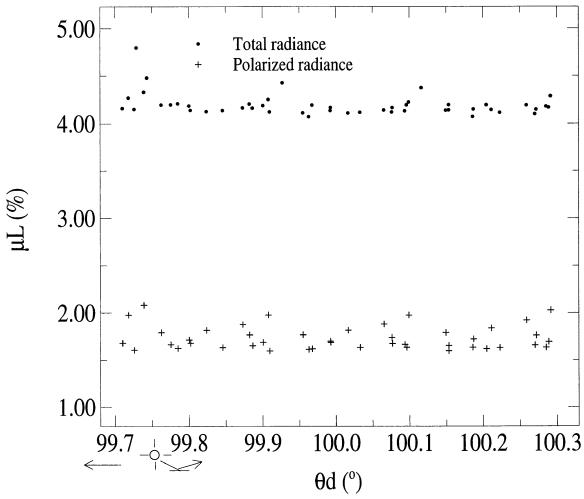

Figure 20. After correction by the airmass, total and polarized radiances, as measured by POLDER on 14 June 1994, are plotted versus the scattering angle θ.

corrections. A good validation of the models used for this objective is illustrated throughout the ground-based measurements.

Polarized Reflectance

We investigate now the possibility of identifying an SF model using the polarized reflectance at 870 nm we measured with POLDER. First, because we believe that the polarization is quite sensitive to the aerosol model, we may have a better sensitivity to the polarization compared to the sensitivity to ε'. Second, for ocean Case 2, the water turbidity in sediments makes quite questionable the darkness of the ocean at 670 nm (Dilligeard et al., 1998). In this last case, the so-called "bright pixel method" (Aiken et al., 1995) is an alternative solution, with some limitations based on *a priori* assumptions such as the spectral dependence of the sediment signature.

Table 10. Selected POLDER Measurement at 850 nm, for a Given Scattering Angle (100° for 14 June; 110° for 13 June and 8 July[a]

	13 June 1994		*14 June 1994*		*8 July 1995*	
	τ_a	$\mu_v L_{pol}$	τ_a	$\mu_v L_{pol}$	τ_a	$\mu_v L_{pol}$
Measured	0.07	0.30	0.207	1.6	0.319	1.1
T70	0.09	0.39	0.38	1.4	0.23	1.1
T90	0.10	0.41	0.42	1.5	0.29	1.2
T98	0.11	0.40	0.45	1.4	0.33	1.2
C70	0.14	0.29	0.56	1.0	0.45	0.8
C90	0.21	0.31	0.85	1.1	0.76	1.2
C98	0.29	0.32	1.12	1.1	1.07	1.1
M70	0.16	0.27	0.63	0.87	0.53	0.69
M90	0.25	0.30	1.01	0.99	0.91	0.92
M98	0.35	0.31	1.46	1.08	1.35	1.03

[a] The difference in azimuth was 60°. For the 9 SF models, we retrieved τ_a to match the measurement radiance. Then we computed the polarized radiance.

The principle of the model selection is the following. Except around the neutral points, the behavior of the atmospheric polarized reflectance with the geometry is quite simple: If we correct for the air mass (multiplying by μ_v), it increases with the scattering angle up to about 90–100°. We applied a sunglint mask first before selecting the total and polarized reflectances at this angle. As it is illustrated in Figure 20, after correction by μ_v, the signal selected in a small range of the scattering angle is constant. We then loop for the nine SF models on the aerosol optical thickness in order to retrieve the total radiance. With the corresponding value of τ_a, we compute the polarized reflectance to compare with the measurements. These results are reported in Table 10. The conclusions we draw here are not definitive, but it seems that, for each day, several candidates are capable of retrieving the measurements at 870 nm. This point is, of course, emphasized if we introduce the error bars. For 14 June a relative uncertainty of 6% for the absolute calibration results in $\Delta\tau_a = \pm 0.05$ and a resulting error on the polarized radiance of 0.1. On the other hand, the measurements themselves are quite scattered. This crude analysis seems to indicate that the use of the polarized radiance at 870 nm does not bring much in the model selection than ε'.

CONCLUSION

This article presents results of field experiments occurring in 1994 and 1995 in the Straits of Dover. Two very different temporal periods were chosen for ocean color analysis purposes. The summer situation (June 1994 and July 1995) was favorable to remotely sense chlorophyll pigment whereas fall equinox tides (October 1994) were favorable to remote-sense resuspended particles from the bottom. Moreover, ocean–atmosphere interaction involves specific meteorological conditions widely different according to the season. The POLDER instrument was introduced for the first time above the site of measurements in an airborne version and acquired numerous scenes. At the same time, ground-based radiometers performed atmospheric optical measurements. A complete description of the atmosphere was conducted using both kinds of data. Spectral aerosol variation of sky radiance and the degree of polarization were studied in order to derive aerosol refractive index and size distribution. An unexpected behavior of the degree of polarization at 1650 nm and a strong variation of the Gordon coefficient revealed an aerosol model more complex than a size distribution law with one parameter. Assumptions of several modes of particles in the atmosphere were tested and issued acceptable results. A submicrometric mode of maritime particles mixed to continental rejections allowed to retrieve sky measurements. Moreover, the usual Shettle and Fenn models, developed for SeaWifs algorithm, also retrieved these ground

measurements. These models are rigorously different from the SF models retrieved from airborne data. Nevertheless, a comparison of their atmospheric functions showed that ground-based measurements represent a good way of validating the models used to proceed to atmospheric corrections.

A good example of the complexity of the coastal waters medium is illustrated here. It is difficult to parametrize atmosphere with simple size distribution laws, but applications of SF models are sufficient to retrieve aerosol nature.

We first thank J. L. Deuzé and P. Goloub for all the helpful scientific discussions we had all over this work. They also both participated to the experiments helped by Y. Balois, P. Lecomte, and C. Verwaerde, all of them from LOA. The computer assistance was provided by D. Dessailly. We also thank the Nord-Pas de Calais region for financial contribution to the Dyscop program, the EC through the Flux-Manche-2, a MAST program, and to a lesser extent the CNRS with some support from the PNTS program.

REFERENCES

Aiken, J., Moore, G. F., Trees, C. C., Hooker, S. B., and Clark, D. K. (1995), The SeaWiFS CZCS-type pigment algorithm, SeaWiFS Technical Report Series: Volume 29. NASA Technical Memorandum 104566, NASA Goddard Space Flight Center, Greenbelt, MD.

André, J. M., and Morel, A. (1991), Atmospheric corrections and interpretation of marine radiances in CZCS imagery. *Oceanol. Acta* 14:3–22.

Bentley, D. (1985), Caractéristiques physico-chimiques des eaux du détroit du Pas de Calais. *J. Rech. Océanogr.* 10(2):69–71.

Bricaud, A., and Morel, A. (1987), Atmospheric corrections and interpretation of marine radiances in CZCS imagery: use of a reflectance model. *Oceanol. Acta* 7:33–50.

Brylinski, J. M., Lagadeuc, Y., Gentilhomme, V., et al. (1991), Le "fleuve côtier": un phénomène hydrologique important en Manche Orientale. Exemple du Pas de Calais. *Oceanol. Acta* 11:197–203.

Chami, M., Santer, R., Deuzé, J. L., and Goloub, P. (1995), Aerosol remote sensing using the POLDER instrument. Results of a campaign over the Straits of Dover. *In Proceedings SPIE Satellite Remote Sensing II*, Paris, September, pp. 2–12.

Cosnefroy, H., Briottet, X., Leroy, M., Lecomte, P., (1997), A field experiment in Saharian Algeria for the calibration of optical satellite sensor. *Int. J. Remote Sens.* 18(16):3337.

Deschamps, P. Y., Bréon, F. M., Leroy, M., et al. (1994), The POLDER mission: instrument characteristics and scientific objectives. *IEEE Trans. Geosci. Remote Sens.* 32(3):598– 615.

Deuzé, J. L., Devaux, C., Herman, M., and Santer, R. (1988), Aerosol remote sensing from ground-based polarization measurements. *In Proceedings of the International Radiation Symposium*, pp. 543ff.

Deuzé, J. L., Herman, M., and Santer, R. (1989), Fourier series expansion of the transfer equation in the atmosphere-ocean system. *J. Quant. Spectrosc. Radiat. Transfer* 41(6): 483–494.

Deuzé, J. L, Bréon, F. M., Deschamps, P. Y., et al. (1993), Analysis of the POLDER (POLarization and Directionality of Earth's Reflectances) airborne instrument observations over land surfaces. *Remote Sens. Environ.* 45:137–154.

Dilligeard, E., Santer, R., Chami, M., et al. (1998), Sediment remote sensing in coastal waters using *in-situ* calibration. *Continental Shelf Res.* in press.

Dupont, J. P., Bentley, D., and Richard, A. (1981), Suivi du détroit du Pas de Calais. *J. Rech. Océanogr.* 6(1):16.

Gordon, H. R., and Wang, M. (1994), Retrieval of water leaving radiance and aerosol optical thickness over the oceans with SeaWifs: a preliminary algorithm. *Appl. Opt.* 33(3):663–653.

Hovis, W. A., Clark, D. K., Anderson, F., et al. (1980), Nimbus-7 Coastal Zone Colour Scanner: system description and initial imagery. *Science* 210:60–63.

Junge, C. E. (1952), Gesetznïssigkeinten in der grossenverteilung atmosphäricken aerosols über dem Kontinent. *Ber. Dtsch. Wetterdienst.* U.S. Zone 35, 261.

Schwindling, M. (1996), Modèles et mesures pour l'observation spatiale de la couleur de l'océan: diffusion atmosphérique par les aérosols et réflexion de surface par l'ecume. Thèse, l'Université des Sciences et Technologies de Lille.

Shettle, E. P., and Fenn, R. W. (1979), Models for the aerosols of the lower atmosphere and the effect of humidity variations on their optical properties, AFGL-Rep. TR-79-0214, Air Force Geophys. Lab., Bedford, MA.

Sturm, B. (1981), The atmospheric correction of remotely sensed data and the quantitative determination of suspended matter in marine water surface layer. In *Remote Sensing in Meteorology, Oceanography and Hydrology* (A. P. Cracknell, Ed.), Chichester, Ellis Horwood, pp. 163–197.

WMO (1986), A preliminary cloudless standard atmosphere for radiation computation, Rep. WCP-112 and WMO/TD-NO024, Geneva, March, 53 pp.